



**HAL**  
open science

## Mechanical evolution of an altered limestone using 2D and 3D digital image correlation (DIC)

L. Zinsmeister, J. Dautriat, A. Dimanov, J. Raphanel, Michel Bornert

► **To cite this version:**

L. Zinsmeister, J. Dautriat, A. Dimanov, J. Raphanel, Michel Bornert. Mechanical evolution of an altered limestone using 2D and 3D digital image correlation (DIC). 47th US Rock Mechanics, Geomechanics Symposium, Jun 2013, San Francisco, United States. 16 p. hal-01579348

**HAL Id: hal-01579348**

**<https://enpc.hal.science/hal-01579348>**

Submitted on 25 Apr 2022

**HAL** is a multi-disciplinary open access archive for the deposit and dissemination of scientific research documents, whether they are published or not. The documents may come from teaching and research institutions in France or abroad, or from public or private research centers.

L'archive ouverte pluridisciplinaire **HAL**, est destinée au dépôt et à la diffusion de documents scientifiques de niveau recherche, publiés ou non, émanant des établissements d'enseignement et de recherche français ou étrangers, des laboratoires publics ou privés.

# Mechanical evolution of an altered limestone using 2D and 3D digital image correlation (DIC)

Zinsmeister, L., and Dautriat, J.

*IFP Energies nouvelles, Rueil Malmaison, 92852, France*

Dimanov, A., and Raphanel, J.

*Ecole Polytechnique, Palaiseau, 91128, France*

Bornert, M.

*Ecole des Ponts ParisTech, Champs sur Marne, 77455, France*

**ABSTRACT:** In the context of long term CO<sub>2</sub> sequestration, we present an original laboratory workflow which allows a multi scale analysis of the effect of a chemical alteration on both petrophysical and mechanical properties of a carbonate. The relation between the mechanical behavior and the microstructural evolutions is investigated using the digital image correlation techniques. For this purpose we imaged intact and altered samples during uniaxial and triaxial mechanical tests using optical microscopy, scanning electron microscopy and 3D X-ray microtomography. The porosity increase induced by homogeneous alteration leads to lower elastic moduli and critical stress at sample failure. Furthermore at a same confining pressure we observed a transition from brittle to ductile failure mechanisms with the increase of alteration level. These observations are evidenced by digital image correlation. Altered samples evidenced early strain localization which was not observed in the intact ones. These early localization events induce more compaction at the macroscopic scale and tend to initiate early fracturing.

## 1. INTRODUCTION

The injection of CO<sub>2</sub> in deep saline aquifer gave rise to the study of carbonates because these reservoirs represent the major storage capacities for this type of storage [1]. The injection of reactive fluids like supercritical CO<sub>2</sub> induces a dissolution which can decrease the storage capacities by fracturing or compaction effects. In the case of long term storage, the CO<sub>2</sub> plume is diluted and homogeneous alteration becomes a major type of dissolution [2]. In this context, the description of the mechanical behavior by a predictive 4D model is necessary to monitor the storage site.

In order to mimic the homogeneous dissolution pattern, Egermann *et al.* [3] developed a protocol based on the use of a retarded acid treatment and applied it for studying the mechanical response. A softening of the material was recorded but could not be attributed only to an increase of porosity [4]. Microstructural effects of the alteration were called to explain this difference but no evidence has been shown in these early studies.

In order to evaluate the influence of the microstructure on the mechanical behavior, digital image correlation (DIC) is a way to detect the strain localization during a loading by imaging a surface (or a volume) during a mechanical loading. This technique has been employed

in 2D on unconsolidated materials [5], in 3D on mudstone [6] using synchrotron radiation allowing the description of shear bands, and on sandstone [7] using a 3D X-ray CT but by *post-mortem* sample comparison. The only use of DIC on carbonates, to the authors knowledge, is found in [8] which is a 2D study of non altered Estailade limestone. This last study, combining optical and SEM data, establishes the feasibility of DIC on materials which sustain very small deformation only such as carbonates. The main results were to evidence the closing of porosity and the brittle fracture development between the microporous parts of the sample.

In this paper we present a multi scale approach coupling 2D optical, 2D Scanning Electron Microscopy (SEM) and 3D microtomography ( $\mu$ -CT) methods. The study is made on the oolitic Lavoux limestone chosen for its simple microstructure: microporous oolites, cement and macroporosity. Our purpose is to determine the influence of the microstructural changes on the mechanical behavior of an altered sample and to seek a link between our observations on carbonates and the better known behavior of sandstone.

## 2. MATERIAL AND METHODS

### 2.1. Microstructural observations of intact samples

The block used to plug cylindrical samples comes from the Lavoux limestone quarry located in the

vicinity of Poitiers in France. The thin section observation, shown in Fig. 1 evidences the micro structure of the material. This material is composed of microporous oolites ranging from 100 to 500  $\mu\text{m}$  (Fig. 1 (a)) in diameter, microporous pellets ranging from 20 to 60  $\mu\text{m}$  in diameter (Fig. 1(b)), bioclasts (Fig. 1(d)). Two kinds of cements are observed; lightly porous syntaxial cement nucleated from echinoderma fragments (Fig. 1(c)) and sparitic cement around the oolites (well identified in Fig. 2).

- Porosity inferred from dry/wet weight and medical scanner X-Ray attenuation,
- Brine permeability,
- Nuclear magnetic resonance (NMR) to estimate the porosity modality,
- High Pressure Mercury Injection (HPMI) to determine the pore throat distribution.

53 cylindrical samples have been scanned to infer their porosities. Each sample is scanned every millimeter along its axis. A mean porosity of each sample is determined from calibration curves of X-Ray attenuation obtained on mono-mineral calcite samples covering a range of known porosities. The porosity varies from 22% to 26%. For the mechanical tests, we selected samples with a mean porosity of  $24 \pm 0.5\%$  and without large local heterogeneities visible on CT-scan slides. The permeability measured on three samples selected for mechanical tests has a mean value of 17.2 mD (Table 1). The discrepancy between scanner and brine porosities can be explained by the occurrence of non connected porosity [9] (Sterpenich *et al*, 2009)

Table 1 Initial permeability and water porosity for three samples.

Sample name	Permeability	Brine Porosity (%)
Z10	17,1	23,8
Z17	17,1	23,6
Z21	19,1	24,2

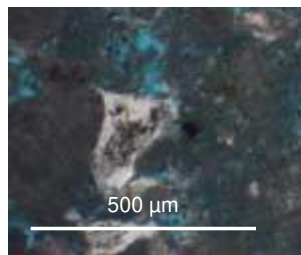


Fig. 1. Thin section of Lavoux limestone in white light microscopy. (a) Oolite (b) Pellet (c) Syntaxial cements (d) Bioclast. The porosity appears in blue due to colored epoxy saturation.

These observations are completed by SEM imaging, confirming the description (Fig. 2). To clearly illustrate this microstructure we present a picture from another block of the same material which contains larger grains and pores. We notice the variability of the microporosity contained in the oolites and the smooth surface of the sparitic cement.

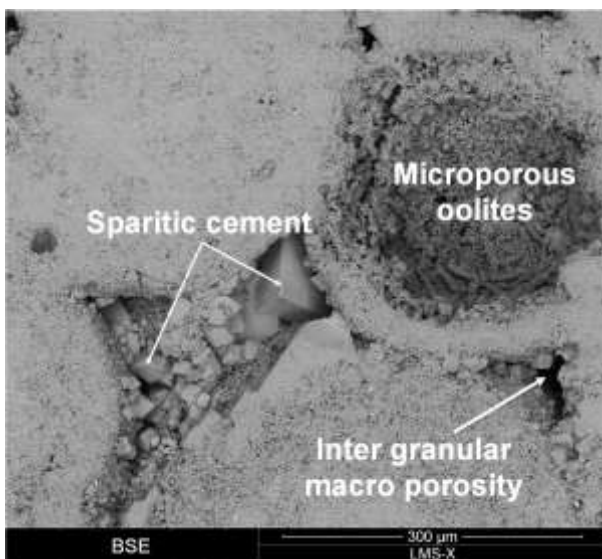


Fig. 2. SEM micrograph of polished section of the Lavoux limestone.

### 2.2. Petrophysical description of intact samples

This characterization is based on several laboratory petrophysical methods

The T2 time relaxation curve obtained from NMR measurement on a sample saturated by 20 g/l NaCl brine is presented Fig. 3. Instead of two expected peaks from the microstructural description, the NMR signal is unimodal. This phenomenon had been explained by a diffusion pore coupling by [10] Vincent *et al*, (2011) and relates to the connectivity between the microporosity and the macroporosity. The two small peak are non consistent with physical reality.

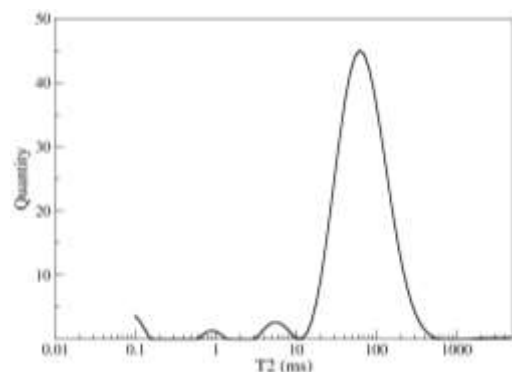


Fig. 3. Distribution of the T2 relaxation time inferred from NMR on the Lavoux limestone.

However the HPMI results pointed a bimodal repartition of the pore throat (Fig. 4), characterized by two peaks at 0.3 and 4  $\mu\text{m}$  corresponding to the micro and the macroporosity pore throat, respectively.

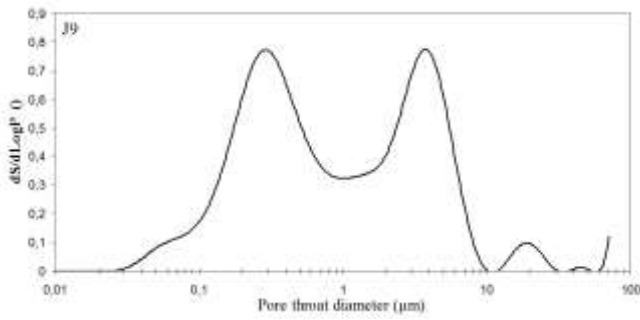


Fig. 4. Distribution of the pore throat diameter obtained by HPMT on an example of the presented limestone.

### 2.3. Alteration protocol

Since all the mechanical tests are destructive, the effect of chemical alteration have to be investigated using companion samples altered prior to the mechanical tests, hence the importance of selection to reduce variability.

The sample alteration technique is based on Retarded Acid Treatment (RAT) following the protocol developed by [3]. This methodology allows a homogeneous alteration of the sample, conversely to CO<sub>2</sub>-brine injection [11, 9, 12, 13, 14]. The experimental set-up is composed of a confining Hassler cell, which allows the application of a hydrostatic stress on the sample isolated of the confining medium by a core sleeve. The intact state permeability is measured at a confining pressure  $P_c = 6$  MPa. Afterwards, the brine is flushed out by the injection of three pore volumes ( $V_p$ ) of an initially inactive acid. The sample is then placed under undrained conditions and the temperature is increased up to 60°C to activate the acidification reaction. When the pore pressure reaches a plateau, usually after one night, the equilibrium between reactive fluid and carbonate is assumed, and the core is flushed by fresh brine. Effluents are collected and the particles size distribution is measured by laser diffraction. The complete protocol is repeated until a chosen number of RAT. Permeability is measured between each RAT. More details on the method and petrophysical results are provided by [15].

### 2.4. Conventional characterization of sample mechanical properties.

The aim of these preliminary experiments is the estimation of static elastic properties and mechanical strengths evolutions due to the alteration. Experiments are performed on brine-saturated samples loaded with a conventional triaxial cell. Axial and radial strains are recorded using strain gages glued on the circumferential surface of the plug. The tests have been performed on series of intact, 3 RAT and 6 RAT companion samples, corresponding to homogeneous porosity increases of 1.2 and 2.4 %.

For each alteration degree, triaxial experiments have been run at 6 MPa, 11 MPa and 16 MPa of confining pressure and at a constant pore pressure of 1 MPa. The elastic moduli, here the Young Modulus and the Poisson's ratio, are estimated at the beginning of the

test during an axial loading/unloading in the elastic domain, at a low confining pressure of 2 MPa Fig. 5(I). Hereafter, the pressure is increased hydrostatically up to one of the values given above Fig. 5(II) and then the triaxial test starts by increasing the axial stress up to the sample failure at constant confining pressure Fig. 5(III). The protocol is schematically presented in the Fig. 5

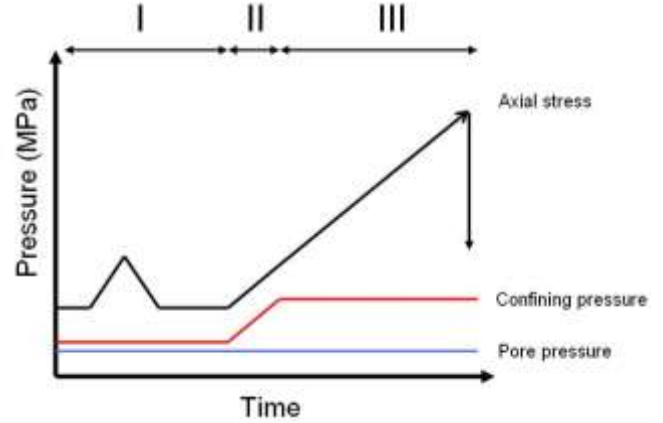


Fig. 5. Triaxial test protocol.

### 2.5. 2D-DIC and 3D-DIC methods

The aim of the DIC method is the determination of the deformation field from the displacement field obtained by the comparison between a reference picture (shot before loading) and pictures acquired at successive stages of a mechanical solicitation [16]. The reference picture is discretized into a grid of points, which is centered on a correlation domain. Each correlation domain is defined by its grey level fluctuations (defined in 8 bits or 16 bits). The DIC is based on the determination of the most similar domain in the deformed picture by the minimization of a correlation criterion with the assumption of a conservation of the grey level distribution during the transformation in these domains. The position of each central point of the domains on the deformed configuration allows the determination of the displacement field. A subpixel resolution on the displacement is obtained by a bilinear interpolation of the grey level in each domain. Because of the small deformation sustained by our geomaterials before failure (~0.5%), we paid particular attention to the acquisition parameters to get the better compromise between displacement field uncertainty and spatial resolution. To estimate these uncertainties, rigid body motions have been performed at the reference stage following the methodology described by [8].

Once the displacement field is obtained as a discrete set of values on the grid of points, the local transformation gradient can be computed by derivation using a scheme which will determine the local gage size. For more details, refer to [17, 18]. With the small strain assumption, the in-plane components of the small strain tensor are thus known. Let  $x$  be the compression axis. It is reasonable to assume that the

normal axis to the observation plane, say z, is a principal axis of deformation and that there is no out of plane rotation, so that  $\epsilon_{zx} = \epsilon_{zy} = 0$ , furthermore assuming axisymmetry  $\epsilon_{yy} = \epsilon_{zz}$ . The equivalent von Mises strain used in this paper can then be deduced using the relation (1).

$$\epsilon_{eq} = \frac{2}{3} \sqrt{(\epsilon_{xx} - \epsilon_{yy})^2 + 4(\epsilon_{xy})^2} \quad (1)$$

By extension the 3D-DIC method is based on the same principle but adding a dimension in the search of the correlation domain which becomes a cube [19] and the measurements are made on a voxel which is the 3D equivalent of a pixel.

As for the 2D-DIC, once the displacement field is obtained, the six components of the small strain tensor can be computed.

## 2.6. Mechanical tests coupled to image acquisitions for DIC post-processing.

The image acquisitions prior to DIC had been obtained for three methods of investigations. In this study, we applied conventional 2D-DIC techniques on optic and SEM images of the surface sample uniaxially loaded and extend this technique to 3D volumes imaged by microtomography, at successive triaxial stress states.

### - Optical tests

The macroscopic compression tests are performed on a uniaxial loading frame controlled in displacement. Cylindrical samples of 35 mm high and 36 mm in diameter are machined to produce two opposite flattened 25 mm wide surfaces. Load and displacement are measured by a strength sensor and a LVDT, respectively. A constant displacement rate of 1  $\mu\text{m/s}$  is imposed until the sample failure. During loading, images of one flattened surface are taken at constant time intervals by a high resolution CCD camera (4872x3248 ~16 Mpixel and 4904x3280 for the second one) covering the whole surface (with pixel size of ~7  $\mu\text{m}$  at x1 magnification). Black and white painting sprays are applied on the imaged surface to enhance local contrast and optimize the DIC efficiency.

### - SEM tests

Small parallelepiped samples (14 mm x 7 mm) are tested inside a SEM equipped with a simple compression rig (maximum load 5 kN). Displacement is controlled at a rate of ~1  $\mu\text{m/s}$ . The SEM image acquisition lasts several minutes; consequently the loading is performed in a stepwise manner. The natural contrast of the material is sufficient for DIC, but the contrast and brightness must be optimized before each acquisition to spread the grey level histogram over the full 16 bit range. The magnification varies from x60 to x80, corresponding to imaged surfaces of 2.1mm x 1.8 mm (5  $\mu\text{m}$  of resolution) and 1.6 mm x 1.4 mm (3.9  $\mu\text{m}$  of resolution).

### - $\mu$ -Tomography tests

The triaxial tests are carried out using a miniaturized triaxial cell developed at IFPEN on small cylindrical samples of 10 mm in diameter and 20 mm in length. The body of the cell is made of aluminum alloy minimizing the absorption of the X-ray emitted by the  $\mu$ -tomograph source. This set up allows the application of a confining pressure up to 15 MPa and a pore pressure, controlled by two independent pumps. The axial load is measured by a sensor and its maximum is 10 kN. The axial stress is manually screw driven. Since the time required for a set of radiograph projection acquisitions takes about 3 hours, the sample is loaded in stepwise manner. The number and the amplitude of load steps are estimated from macroscopic triaxial tests.

The best conditions for image acquisitions and reconstructions have been derived from uncertainty minimization based on rigid body motions [19].

The conditions of radiograph acquisition for the 10-mm diameter sample with a resolution of 5 microns are the following: Magnification x10. Source-object distance 20 mm, source-detector distance 200 mm, 2000x2000 field of view, 120KV, 150 $\mu\text{A}$ , 0.2° angular step. Then, the volumes are reconstructed with respect of 1/4 resolution corresponding to a voxel size of 20 $\mu\text{m}$ . The optimization of the ratio signal/noise to improve DIC efficiency requires a filtering of the volumes using in-house algorithm.

## 3. EFFECT OF ALTERATION

### 3.1. Evolution of the microstructure

The porosity profiles after alteration obtained by CT-scanner validate the homogeneity of the alteration for 3 and 6 RAT (Fig. 6). The mean increase of porosity per RAT is 0.4 % as shown in the Fig. 6. This value is in good agreement with values obtained by the other methods of porosity estimation.

The SEM micrographs of Fig. 7 highlight the apparition on the surface of the sparitic cement of detachment of imbricate minerals (red squares in Fig. 7.b,c,d) and "corrosion pits" (Fig. 7.a) leading to surface roughness not observed on intact samples. The Fig. 7.d is obtained on a 13 RAT sample; we observed an alteration of huge rhombohedra in the crystalline plane.

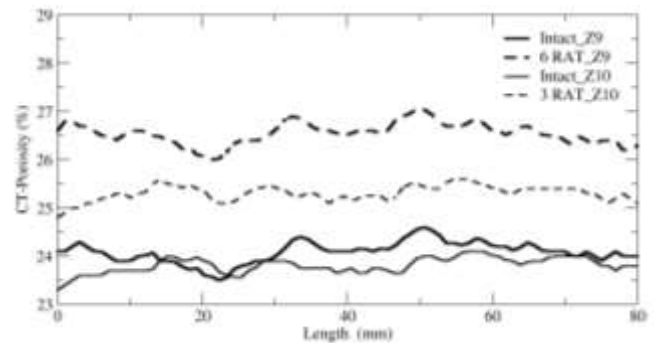


Fig. 6. Porosity evolutions with alteration for two samples used for mechanical tests, Z9 and Z10, altered respectively by 6 and 3 RAT.

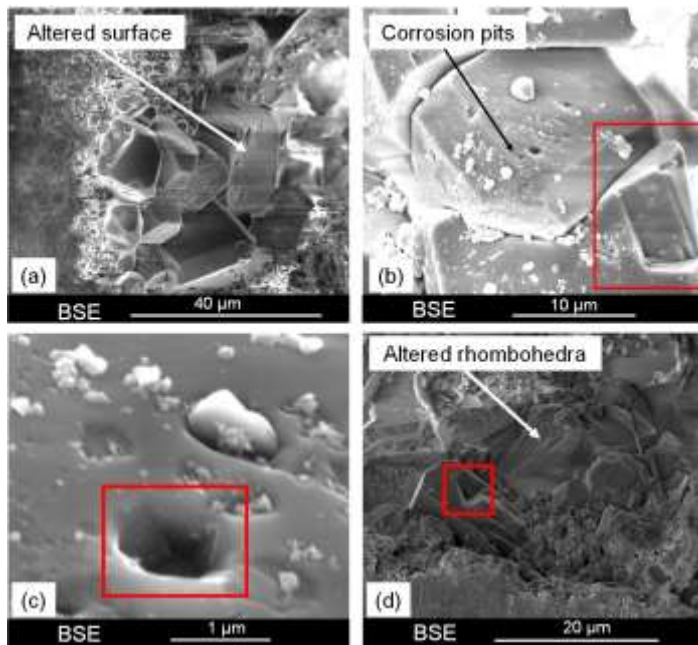


Fig. 7. Altered surface at 2 RAT (a), Detachment of sparitic cement at 2 RAT (b), (c) and 13 RAT (d).

These observations are the only evidences of the alteration at the microscale. However, the mechanisms of corrosion pits formation and particle detachment seem insufficient to explain the increase of porosity with alteration obtained from CT-scanner profiles. We suppose that a part of the micrite at the surface and inside the oolites is dissolved but because of the impossibility to make a before/after alteration in SEM and optical microscope there is no evidence. To validate this assumption we need to image the same sample at different stages of alteration. For instance, [9]Noiriel *et al*, 2004, used X-ray microtomography on small Lerouville carbonate samples and were able to quantify the dissolved calcite after an heterogeneous alteration. However in our case it would take a large number of RAT to reach at least one voxel of dissolution at the interface between pores and grains.

### 3.2. Macroscopic triaxial results

Table 2 summarizes the main results inferred from triaxial tests, performed on intact, 3 RAT and 6 RAT samples.

We recall that elastic moduli  $E$  and  $\nu$  are obtained during a loading/unloading cycle at  $P_c = 2\text{MPa}$ . The confining pressure is then increase up to a chosen value (6, 11 or 16 MPa) to determine the failure stresses. All the tests are performed at a constant pore pressure  $P_p = 1\text{MPa}$ .

$C^*$  and  $Q^*$  correspond to critical effective pressure and critical deviatoric stress at sample failure. They are determined:

- in the brittle regime, at the peak stress,
- in the ductile regime, from the recorded piston velocity.

Since the press is force controlled, at the end of the elastic regime, the velocity of the press increases due to dilatancy or shear development. The failure stress is

then determined at the intersection of the tangents of the velocity in the elastic regime and during the failure propagation as shown in Fig. 8.

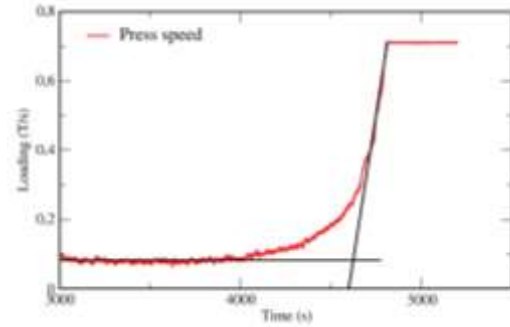


Fig. 8. Evolution of the press velocity with time and method of  $C^*$  and  $Q^*$  determination.

The alteration leads to a diminution of the Young's modulus. The mean Young's modulus is 22.0 GPa for intact sample, 19.2 GPa for 3 RAT and 15.1 GPa for 6 RAT. This weakening can be explained by two factors; on the one hand the increase of the mean porosity, on the other hand the evolution of the microstructure. The contribution of each factor to the global weakening of the material is not obvious at this stage of the study. However, we can assume that the increase of the mean porosity should lead to a linear dependency of the Young's modulus on the alteration, which is not observed here.

Fig. 9 presents the axial and radial deformation recorded by strain gages during triaxial compaction tests, at effective pressures of 5, 10 and 15 MPa (Fig. 9 a,b,c respectively), and for intact, 3 RAT and 6 RAT samples.

Table 2. Mechanical properties inferred from triaxial cell and sorted by RAT number: Initial and after alteration CT-scanner mean porosity, Poisson's ratio, Young's modulus, Mean Young's modulus, confining pressure of triaxial tests, critical effective pressure and critical deviatoric stress

Sample	RAT n°	$\Phi_{ini}$ (%)	$\Phi_{Alt}$ (%)	$\nu$	E (GPa)	E mean (GPa)	Pc (MPa)	Q* (MPa)	C* (MPa)
Z13	0	24,4	24,4	0,26	18,3	22,0	6	32,4	15,7
Z16	0	24,1	24,1	0,28	25,8		11	37,9	22,5
Z18	0	24,2	24,2	0,24	21,9		16	37,3	27,3
Z48	3	23,4	24,6	0,22	19,4	19,2	6	31,6	15,7
Z10	3	23,8	25,3	0,28	20,0		11	29,5	19,9
Z21	3	24,1	25,6	0,25	18,2		16	28,5	24,8
Z9	6	24,1	26,6	0,27	13,4	15,1	6	21,4	12,2
Z11	6	23,7	26,5	0,32	16,5		6	26,2	13,7
Z51	6	23,7	26,1	0,25	14,6		11	24,1	18,3
Z17	6	23,9	26,3	0,24	15,8		16	22,3	22,6

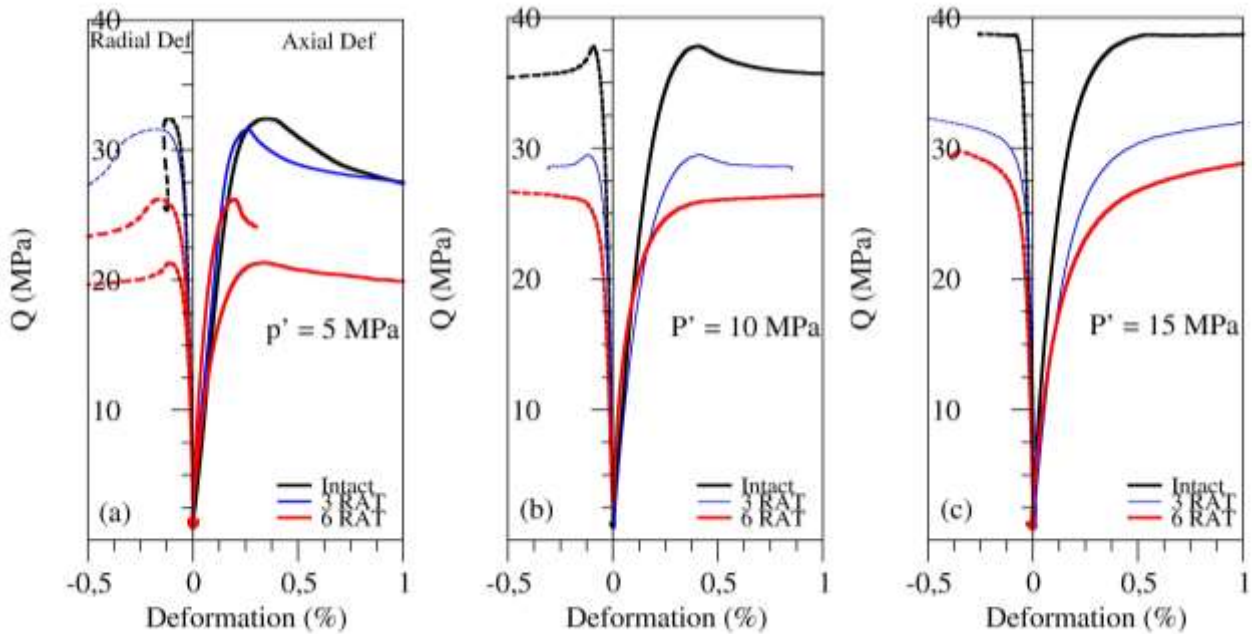


Fig. 9. Radial and axial deformations at given mean effective pressure of (a) 5 MPa (b) 10 MPa and (c) 15 MPa measured by strain gauges.

First of all, the alteration leads systematically to a decrease of the critical stresses. However the sample Z48 (3 RAT, 5 MPa) fails close to the corresponding intact sample probably due to its porosity after alteration only 0.2 % higher (see Table 2). Despite the careful selection of the samples, dispersion in the critical stress level is observed due to the intrinsic nature of carbonates.

At 5 MPa of effective pressure, independently of the alteration level all the samples fail in the brittle regime evidenced by peak stresses (Fig. 9.a). Conversely at 15 MPa, the two altered samples fail in the ductile regime but the intact sample seems to present a weak peak stress (Fig. 9.c). At 10 MPa, intact and 3 RAT samples are still in the brittle regime, but 6 RAT sample exhibits a ductile behaviour (Fig. 9.b).

The Fig. 9 evidences a transition from a brittle regime to a ductile regime (as observed in sandstone by [20, 21, 22] enhanced by the alteration at a given confining pressure.

#### 4. ASSESMENT OF STRAIN HETEROGENEITY BY DIC

##### 4.1. Uniaxial compression of macroscopic samples

We have tested three intact samples, one 3 RAT sample and three 6 RAT samples. We discuss one representative example of each case.

We present (Fig.10 a,b,c) loading curves with the three stages analyzed by 2D DIC.

It was not possible to compare Young's moduli and Poisson's ratio obtained by DIC and strain gauges. A sliding motion effect of the sample induces an over estimate of the axial deformation and an under estimate of the radial one. The mean values of the strain computed by DIC are consequently affected but the strain maps represent the local variations and translate the heterogeneity of the deformation at the local level.

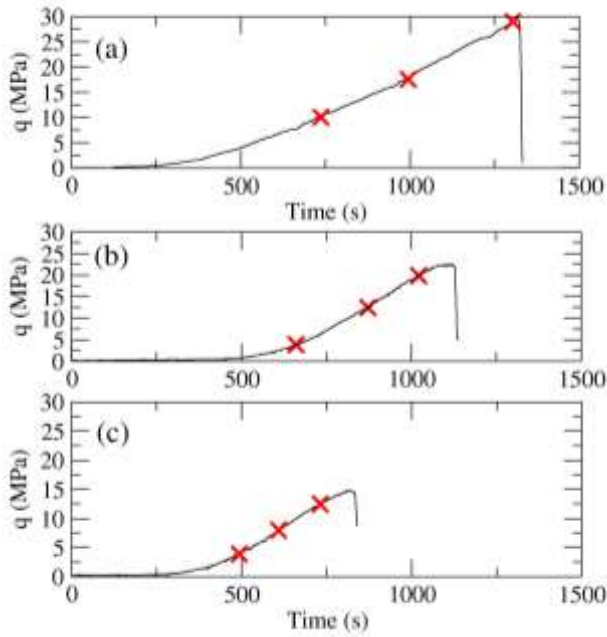


Fig. 10. Loading curves for intact, 3 RAT and 6 RAT samples, denoted (a), (b) and (c) respectively. Red crosses point out the loading stages for which the strain map are presented in the Fig. 11, 12 and 13.

The in-plane strains  $\epsilon_{11}$ ,  $\epsilon_{22}$  and  $\epsilon_{eq}$  maps for intact and altered samples at three different stages of loading and alterations are presented in Fig. 11, 12 and 13. The objective is to determine if the changes of Young's moduli recorded by gages are only linked to the increase of porosity in which case the axial strain would be rather homogeneous or if the evolutions of the microstructure described in section 4.1 also influence the mechanical behavior of the rock in which case one expects more local heterogeneities.

The intact samples present a mean deformation before the failure of  $\sim 0.2\%$ . The failure comes suddenly, and the UCS ranges from 26 to 32 MPa. The analysis of  $\epsilon_{11}$  and  $\epsilon_{22}$  maps for the sample B (Fig. 11) taken as example, can be sequenced as follow. At 10.1 MPa, the strain is uniform ( $\epsilon_{11} \sim -0.02\%$ ) as expressed by a light blue color. At 17.6 MPa,  $\epsilon_{11} \sim -0.04\%$ , some spots present higher deformation levels (0.2%), seemingly at random. Finally at 29.0 MPa the  $\epsilon_{22}$  map shows clearly that tensile cracks develop linking the previously noticed spots.

As shown in the Fig. 12, the 3 RAT sample presents at 3.9 MPa a very low uniform axial deformation of 0.02 %, further in the loading (12.5 MPa) we observe a higher mean deformation ( $\epsilon_{11} > 0.15\%$ ) and localization of  $\epsilon_{11}$  in horizontal compression patterns, and no significant transverse deformation  $\epsilon_{22}$ . Finally at 19.9 MPa (2.3 MPa from failure) the mean axial deformation is up to 0.23% and the initial localization has developed into "compaction bands". The  $\epsilon_{22}$  map shows that local cracks appear at the top

right of the sample leading to one of the final failure pattern.

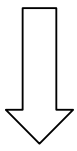
The microstructure events are characterized by a more important pore closure and a more continuous failure than the intact sample. The initiation of the failure is more visible.

At similar stress (4 MPa), the 6 RAT samples (Fig. 13) highlight a mean axial deformation of 0.1 % and a compaction localization in the top left of the sample: while the  $\epsilon_{22}$  map is uniform. At 8 MPa, the mean axial deformation equal to 0.2% and the initial localization has developed. There are also some localized zones on the  $\epsilon_{22}$  map. At the top right, initiation of crack opening is visible. Finally, at 12.5 MPa (2 Mpa from failure) the mean deformation has not increased but there is a wide "compaction band" and in the  $\epsilon_{22}$  map large cracks are visible.

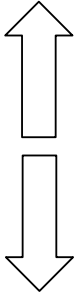
A more detailed study of the microstructure at the strain localization leads to the description of the local type of deformation mechanisms. One part of the deformation is due to microcracking events leading to a major crack where "cataclastic" events are observed at the top left. Where there is no local deformation, the sample deforms uniformly by pore compression.

In conclusion, the three kinds of samples present contrasting deformation patterns. The intact one develops progressively an interconnected network of shear bands leading to the development of diffuse micro damages until the peak stress. The 3 RAT sample is quite similar but presents a higher compressive behavior with more visible "compression bands" until the failure. Similarly the 6 RAT samples demonstrate a higher mean compressibility. Furthermore we observe some micro cracks apertures while loading the 6 RAT sample, which can explain the higher mean deformation and the non elastic deformation coupled to cataclastic events.

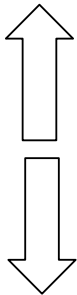
The microstructural clues observed at the macroscale have to be confirmed at the microscale. To this end, the results at the SEM scale are presented in the next section.



$\epsilon_{11}$



$\epsilon_{22}$



$\epsilon_{eq}$

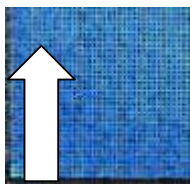
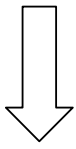
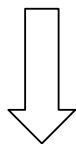
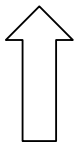
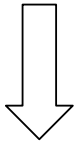
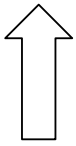


Fig. 11. In-plane strain components  $\epsilon_{11}$ ,  $\epsilon_{22}$  and  $\epsilon_{eq}$  maps for intact sample, at loading stages 10.1, 17.6 and 29.0 MPa reported in the Fig. 10. Grid size = 2813 x 4583 pixels. Measurements basis of 56 pixels = 424  $\mu\text{m}$ .



$\epsilon_{11}$



$\epsilon_{eq}$

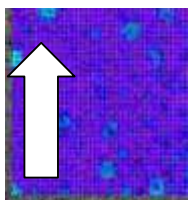
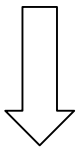
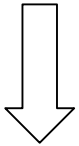
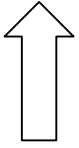


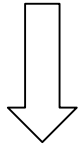
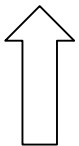
Fig. 12. In-plane strain components  $\epsilon_{11}$ ,  $\epsilon_{22}$  and  $\epsilon_{eq}$  maps for 3RAT sample, at loading stages 3.9, 12.5 and 19.9 MPa reported in the Fig. 10. Grid size = 2813 x 4583 pixels. Measurements basis of 56 pixels = 424  $\mu\text{m}$ .



$\epsilon_{11}$



$\epsilon_{22}$



$\epsilon_{eq}$

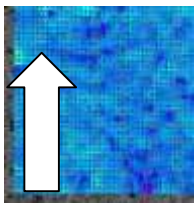


Fig. 13. In-plane strain components  $\epsilon_{11}$ ,  $\epsilon_{22}$  and  $\epsilon_{eq}$  maps for 6RAT sample, at loading stages 4.0, 8.0 and 12.5 MPa reported in the Fig. 10. Grid size = 2813 x 4583 pixels. Measurements basis of 56 pixels = 424  $\mu\text{m}$ .

#### 4.2. 2D SEM microscopic scale results

Fig. 15 presents the position of the initial grid chosen for the two examples presented in the following and the axial load in MPa in function of the displacement measured by external LVDT.

The intact sample (Fig. 16) presents a mean equivalent deformation map dominated by Moiré's pattern traducing a small mean deformation and a slight effect of out-of plane displacement. Small errors are due to the polished oolites surface without good local contrast. Nevertheless, the mean calculated deformation is above 0.2%. Even near the failure value (32.2 MPa) the only microstructural clues of deformation is a closure of the porosity. These observations are in good correlation with the 2D-DIC.

Fig. 17 present  $\epsilon_{11}$  and  $\epsilon_{22}$  maps for a 6 RAT sample at 8.8 MPa and 12.6 MPa of loading. The main result is the early appearance of microcracks, as well as porosity closure. Besides tensile microcracking visible on the  $\epsilon_{22}$  map (inside the white rectangle, Fig. 17.d), we also observe apparently compressive localizations on the  $\epsilon_{11}$  map (inside the white rectangle, Fig. 17.b), which actually represents grain overlapping. Micro previously described cracks initiates and develops at grain interfaces (Fig. 14.b) or in the grains (Fig. 14.a).

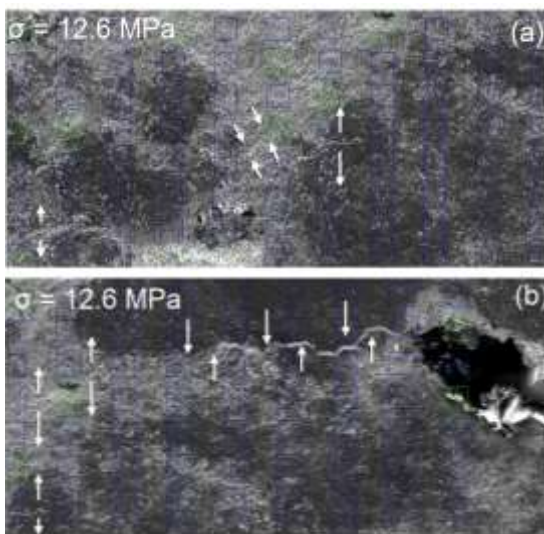


Fig. 14. (a) Extensive and compressive cracks and (b) Extensive cracks developed at grain interface in area reported on Fig. 7. (b) Whites arrow directions highlight the opening or closure of cracks.

This type of continuous strain accommodation is consistent with optical results and can explain the lower resistance of the altered sample and the more diffuse accommodation at macro scale. These observations had been made on 10 intact samples and three 6 RAT samples.

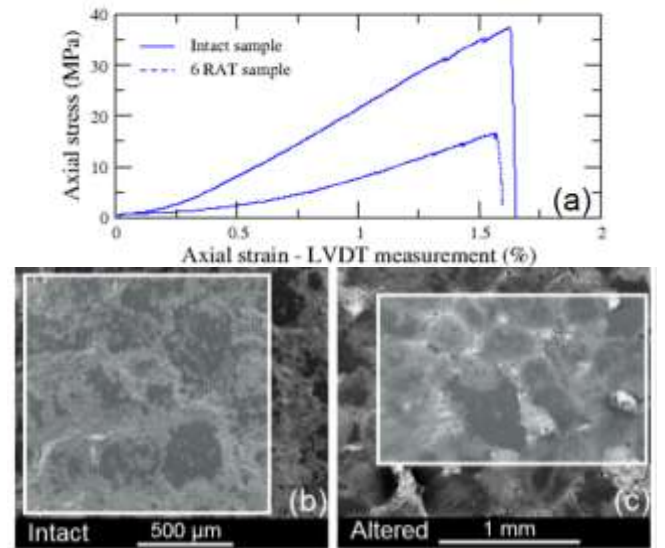


Fig. 15. (a) Stress-strain curves obtained on intact and 6 RATs small sample in the SEM, examples of (b) intact sample and (c) 6 RATs sample reference images acquired at magnification X60 and X80, respectively. The white areas correspond to reference grids.

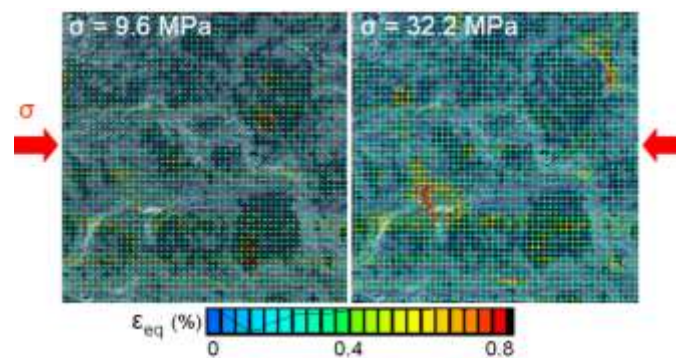


Fig. 16. Equivalent deformation maps for intact sample at 9.6 and 32.3 MPa. Grid size : 3100 x 3046 pixels and measurements basis : 18 µm.

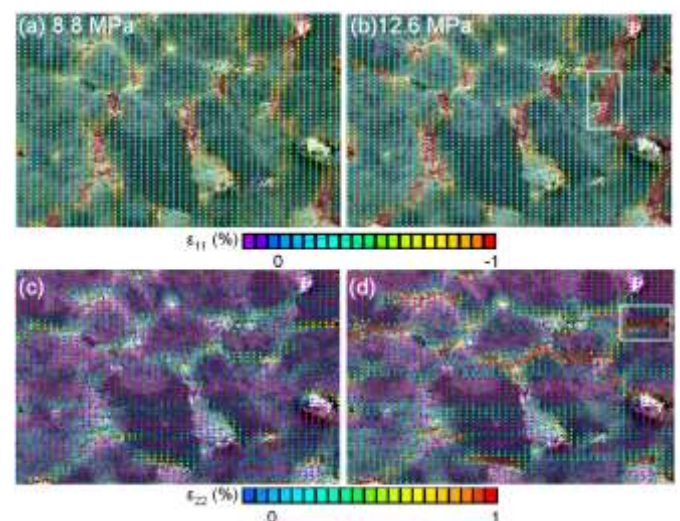


Fig. 17. In-plane strain components (a, b)  $\epsilon_{11}$  and (c, d)  $\epsilon_{22}$  maps of 6 RATs sample at 8.8 and 12.6 MPa. Grid size : 3452 x 1899 pixels, measurements basis : 29 µm.

### 4.3. 3D X-ray microtomography DIC

Uniaxial tests had been performed on intact samples under  $\mu$ -CT and the results were the same than those of 2D DIC presented in the previous sections: no early deformations were visible until the peak stress and the fracture development.

In this section, we focus on two triaxial tests in  $\mu$ -CT made at a confining pressure of 5 MPa, on an intact and a 6 RAT altered sample.

#### - Intact sample

First of all we present the loading curve for the intact sample (Fig. 18)

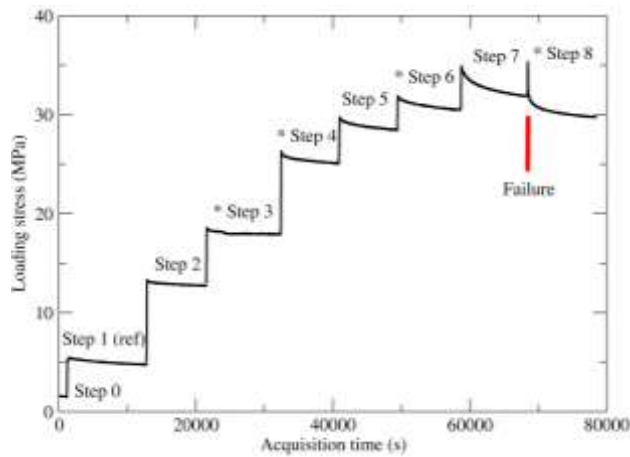


Fig. 18. Loading curve of the test performed on the intact sample at a confining pressure of 5 MPa. The steps pointed out by a star correspond to ones reported in Fig. 20

The intact sample presents a mean deformation of 0.05% at the beginning of the loading and up to 0.2% before the failure. No localization is visible on the intact sample at 18 MPa and the mean axial deformation is low ( $\epsilon_{11} = 0.07\%$ ), at 31MPa the strain remains almost uniform and  $\epsilon_{11} \sim 0.15\%$ . The failure occurs at 36 MPa with an instantaneous appearance of localized fracture consistent with a brittle behavior. This is similar to the previous observations in 2D and triaxial press results.

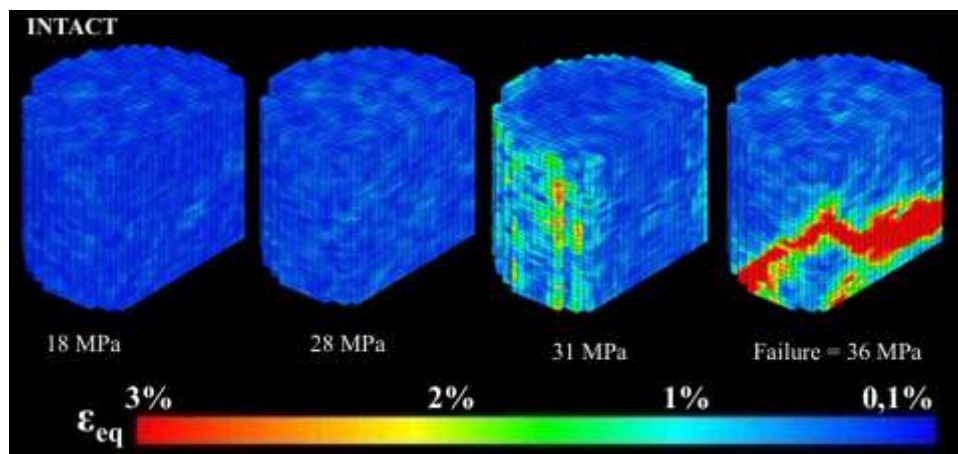


Fig. 20. 3D Equivalent deformation maps obtained for the intact sample subjected to a triaxial compression test at 5MPa of confining pressure. The axial stress level of each presented step is reported in the Fig. 18.

#### - 6 RAT sample

Fig. 19 presents the loading curve for the 6RAT sample

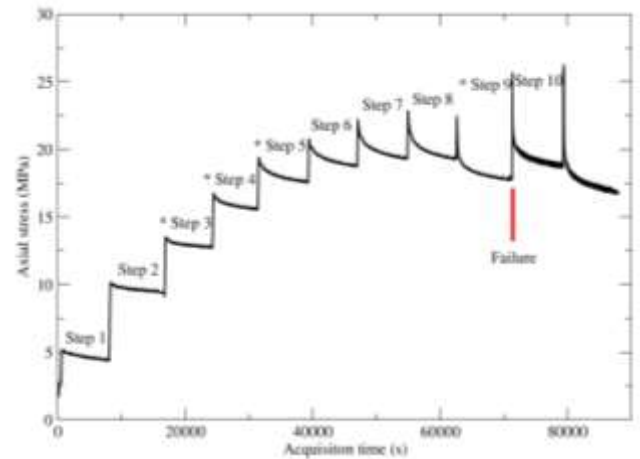


Fig. 19. Loading curve of the test performed on the 6 RAT sample at a confining pressure of 5 MPa. The steps pointed out by a star correspond to ones reported in Fig. 20

The mean deformation at 13 MPa is estimated at 0.1%, it is up to 0.2% at 15 MPa, 0.3% at 20 MPa and 1.6% at 23 MPa. White arrows point to a localization occurring at an early stage of loading and developing in size and intensity (local deformation ranging from 1 % to more than 3 %). The failure is not clearly visible on the loading map and has occurred between step 9 (23 Mpa) and step 10 (25 MPa). The sample has exhibited behavior close to ductile. Fig. 22 proposed an interpretation of the observed discrepancy of failure mechanisms between the intact and 6RAT samples. Whereas the intact sample shows patterns of conventional brittle failure, we suppose that the strong and the highly deformed area is probably a part of a larger undefined band which has not fully developed within the imaged zone. Indeed, we have not be able to find the patterns usually associated to shear bands or compaction bands in sandstone, i.e. localized grain crushing and cataclastic flow surrounded by undamaged zones.

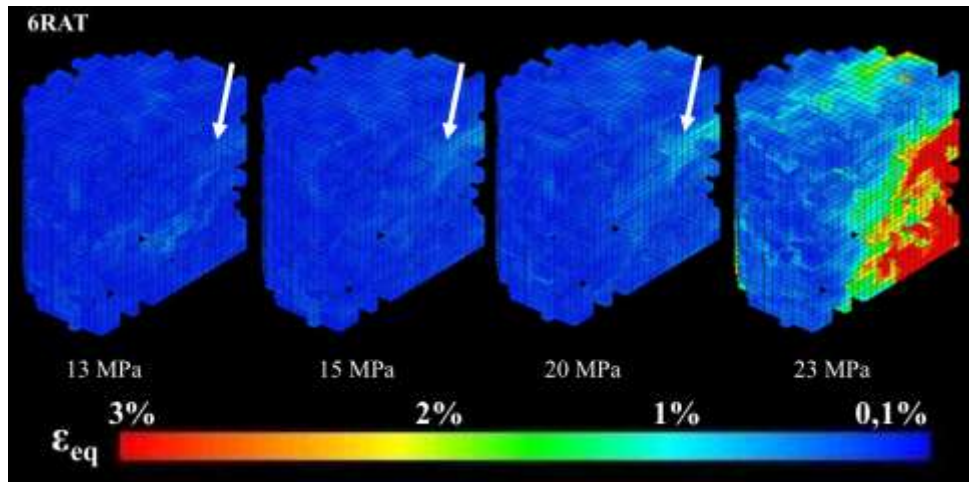


Fig. 21. 3D Equivalent deformation maps obtained for the 6RAT sample subjected to a triaxial compression test at 5MPa of confining pressure. The axial stress level of each presented step is reported in the Fig. 19.

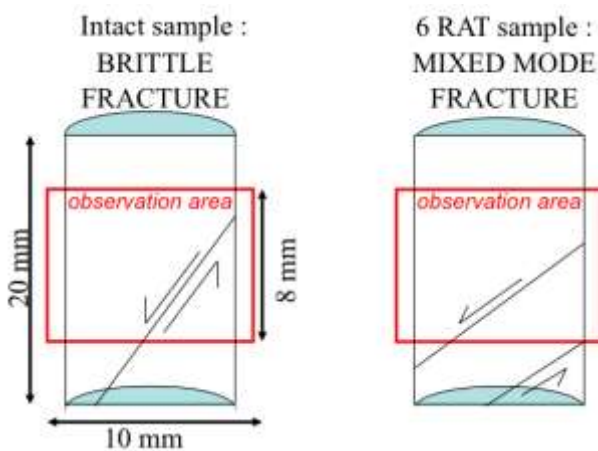


Fig. 22. Schematic interpretation of the failure propagation of the intact and 6RAT samples with respect to the observed area.

## CONCLUSIONS

This paper presents an integrated methodology to understand the effects of a chemical alteration on the mechanical behavior of a carbonate. Since the microstructure evolutions act as a key parameter on the macroscopic properties of the sample, this methodology is based on a multi-scale analysis combining standard triaxial characterization and recent advances in 2D and 3D Digital Image Correlation techniques.

A systematic study of the alteration effects on the mechanical behavior of a carbonate requires two main precautions:

- The samples should be selected on the basis of their structural homogeneity and in a range of equivalent porosity.
- The alteration should not induce heterogeneities to consider companion samples as Representative Elementary Volumes for mechanical tests.

We show that the alteration using a Retarded Acid Treatment leads to an homogeneous sample porosity increase. However, the

microstructural evolutions are mostly controlled by the nature of the grains which may induce local heterogeneous patterns.

The alteration clearly impacts both elastic properties and the failure regime during triaxial compression tests. For a same confining pressure, we notice a shift from a brittle fracture regime to a ductile regime according to the level of alteration.

The impact of the microstructure evolution on macroscopic weakening and mechanical strength has been clearly identified by multi-scale DIC technique. For the first time, we imaged by X-Ray microtomography a compressed carbonate sample in a miniaturized triaxial set-up and used 3D-DIC to interpret the reconstructed volumes. We show different strain accommodation patterns according to the degree of alteration. In uniaxial conditions, intact samples exhibit a diffusive and homogeneous accommodation of the strain before sudden failure propagation. This behavior is mainly due to low deformation at the microstructural scale. Conversely, the altered samples sustain higher deformation levels and exhibit successive strain localization events. At the lower scale, the altered material show a gradual damage characterized by nucleation of microcracks at the grain contacts and their propagation within the grains. The 3D-DIC appears as a powerful and promising tool to better understand the micro-mechanisms of strain localization during a triaxial compression test, and in the context of our study, to characterize the change of failure regime with the level of alteration.

## REFERENCES

1. Bachu, S., and Adams, J. J. (2003). Sequestration of CO<sub>2</sub> in geological media in response to climate change: capacity of deep

- saline aquifers to sequester CO<sub>2</sub> in solution. *Energy Conversion and Management*, 44(20), 3151-3175.
2. André, L., Audigane, P., Azaroual, M., and Menjoz, A. (2007). Numerical modeling of fluid–rock chemical interactions at the supercritical CO<sub>2</sub>–liquid interface during CO<sub>2</sub> injection into a carbonate reservoir, the Dogger aquifer (Paris Basin, France). *Energy Conversion and Management*, 48(6), 1782-1797.
  3. Egermann, P., Bemer, E., and Zinszner, B. (2006). An experimental investigation of the rock properties evolution associated to different levels of CO<sub>2</sub> injection like alteration processes. Paper SCA 2006-34, *Proceeding of the international Symposium of the Society of core Analysts*, Trondheim, Norway, 12-16
  4. Bemer, E., and Lombard, J. M. (2009). From Injectivity to Integrity Studies of CO<sub>2</sub> Geological Storage. *Oil & Gas Science and Technology – Revue de l’Institut Français du Pétrole*, 65(3), 445-459.
  5. Adam, J., Urai J.L., B. Wienke, O. Oonken, K. Pfeifer, N. Kukowski, J. Lohrmann, S.Hoth, W. Van Der Zee, J. Schmatz. 2005. Shear localization and strain distribution during tectonic faulting – new insights from granular flow experiments and high-resolution optical image correlation techniques. *J. Struct. Geol.*, 27: 283 – 301.
  6. Lenoir, N., M. Bornert, J. Desrues., and G.Viggiani. 2007. Volumetric Digital Image Correlation Applied to X-ray Microtomography Images from Triaxial Compression Tests on Argillaceous Rock. *Strain*. 47:193-205.
  7. Louis, L., T.F. Wong, and P. Baud. 2007. Imaging strain localization by X-ray radiography and digital image correlation : Deformation bands in Rothbach sandstone. *J. Structural Geology*. 29:129-140.
  8. Dautriat, J., M. Bornert, N. Gland, A. Dimanov, and J. Raphanel. 2011. Localized deformation induced by heterogeneities in porous carbonate analysed by multi-scale digital image correlation: *Tectonophysics*. 503(1-2): 100-116.
  9. Sterpenich, J., J. Sausse, J. Pironon, A Géhin, G. Hubert, E Perfetti, and D. Grgic. 2009. Experimental ageing of oolitic limestones under CO<sub>2</sub> storage conditions. *Chemical Geology*. 265(1-2): 99-112.
  10. Vincent, B., M. Fleury, Y. Santerre and B. Brigaud. 2011. NMR relaxation of neritic carbonates : An integrated petrophysical and petrographical approach. *J. Applied Geophys.* 74 (1): 38-58.
  11. Noiriél, C., D. Bernard, P. Gouze, and X. Thibault. 2005. Hydraulic Properties and Microgeometry Evolution Accompanying Limestone Dissolution by Acidic Water. *Science And Technology*. 60(1): 177-192.
  12. Bazin, B. 2001. From matrix acidizing to acid fracturing: A laboratory evaluation of acid/rock interactions: *Old Production & Facilities*, 16(1): 22–29.
  13. Le Guen, Y., R. Hellmann, M. Collombet, J.P Gratier, E. Brosse, and I. Fran. 2007. Enhanced deformation of limestone and sandstone in the presence of high PCO<sub>2</sub> fluids: *Earth*, 112.
  14. Daccord, G., E. Touboul, and R. Lenormand. 1989. Carbonate Acidizing: Toward a quantitative model of the wormholing phenomenon: *SPE production engineering*. 63-68.
  15. Zinsmeister, L., J. Dautriat, N. Gland, A. Dimanov, M. Bornert, and J. Raphanel. 2010. Mechanical behavior of an altered reservoir limestone: multi-scale and core analysis approaches. In *Proceedings of Society of Core Analysts. Aberdeen, 27 – 30 August 2012*.
  16. Sutton, M. A., J. J. Orteu, and H. Schreier. 2009. *Image correlation for shape, motion and deformation measurements: Basic Concepts, Theory and Applications*. Springer.
  17. Dautriat, J., 2009. Comportement hydromécanique des roches réservoirs sous contraintes: Relations entre évolution de perméabilité et échelles des mécanismes d’endommagement. PhD, Ecole Polytechnique, France.
  18. Bourcier, M., M. Bornert, A. Dimanov, E. Héripré, and J. L Raphanel. 2013. Multiscale experimental investigation of crystal plasticity and grain boundary sliding in synthetic halite using digital image correlation. *J. Geophys. Res.* In press.
  19. Bornert, M., J. M., Chaix, P. Doumalin, J. C. Dupré, T. Fournel, D. Jeulin, E. Maire, M. Moreaud and H. Moulinec. 2004. Mesure tridimensionnelle de champs cinématique par imagerie volumique pour l’analyse des matériaux et structures. *Photomécanique*. 43-88.
  20. Wong, T.-F., C. David, and W. Zhu. 1997. The transition from brittle faulting to cataclastic flow in porous sandstones: Mechanical deformation: *J. Geophys. Res.*, 102(B2): 3009-3025.

21. Zhu, W. 1997. Shear-enhanced compaction in sandstone under nominally dry and water-saturated conditions. *International Journal of Rock Mechanics and Mining*, 34(364): 3-4.
22. Wong, T.-F., and P. Baud. 2012. The brittle-ductile transition in porous rock: a review. *J. Struct. Geol.* 44: 25-53.